

A transportable hyperspectral imaging setup based on fast, high-density spectral scanning for *in situ* quantitative biochemical mapping of fresh tissue biopsies

Luca Giannoni,^{a,b,†,*} Marta Marradi,^{a,b,†} Kevin Scibilia,^c Ivan Ezhov,^c Camilla Bonaudo,^d Angelos Artemiou,^e Anam Toaha,^{a,b}, Frédéric Lange,^e Charly Caredda,^f Bruno Montcel,^f Alessandro Della Puppa,^d Ilias Tachtsidis,^e Daniel Rückert,^{c,g} and Francesco Saverio Pavone^{a,b,h}

^a University of Florence, Department of Physics and Astronomy, Florence, Italy

^b European Laboratory for Non-Linear Spectroscopy, Sesto Fiorentino, Italy

^c Technical University of Munich, TranslaTUM - Center for Translational Cancer Research, Munich, Germany

^d Azienda Ospedaliero-Universitaria Careggi, University of Florence, Neurosurgery, Department of Neuroscience, Psychology, Pharmacology and Child Health, Florence, Italy

^e University College London, Department of Medical Physics and Biomedical Engineering, London, UK

^f Univ Lyon, INSA-Lyon, Université Claude Bernard Lyon 1, UJM-Saint Etienne, CNRS, Inserm, CREATIS UMR 5220, Lyon, France

^g Imperial College London, Department of Computing, London, UK

^h National Research Council, National Institute of Optics, Sesto Fiorentino, Italy

Abstract

Significance: Histopathological examination of surgical biopsies, such as in glioma and glioblastoma resection, is hindered in current clinical practice by the long times required for the laboratory analysis and pathological screening, typically taking several days or even weeks to be completed.

Aim: We propose here a transportable, high-density, spectral-scanning based hyperspectral imaging (HSI) setup, named HyperProbe1, that can provide *in situ*, fast biochemical analysis and mapping of fresh surgical tissue samples, right after excision, and without the need of fixing, staining nor compromising the integrity of the tissue properties.

Approach: HyperProbe1 is based on spectral scanning via supercontinuum laser illumination filtered with acousto-optic tuneable filters. Such methodology allows the user to select any number and type of wavelength bands in the visible and near-infrared range between 510 and 900 nm (up to a maximum of 79), and to reconstruct 3D hypercubes composed of high-resolution (4-5 μm), widefield images (0.9x0.9 mm^2) of the surgical samples, where each pixel is associated with a complete spectrum.

Results: The HyperProbe1 setup is here presented and characterised. The system is applied on 11 fresh surgical biopsies of glioma from routine patients, including different grades of tumour classification. Quantitative analysis of the composition of the tissue is performed via fast spectral unmixing to reconstruct mapping of major biomarkers, such as oxy- (HbO₂) and deoxyhaemoglobin (HHb), as well as cytochrome-c-oxidase (CCO). We also provided a preliminary attempt to infer tumour classification based on differences of composition in the samples, suggesting the possibility to use lipid content and differential CCO concentrations to distinguish between lower and higher grade gliomas.

Conclusions: A proof-of-concept of the performances of HyperProbe1 for quantitative, biochemical mapping of surgical biopsies is demonstrated, paving the way for improving current post-surgical, histopathological practice via non-destructive, *in situ* streamlined screening of fresh tissue samples in a matter of minutes after excision.

Keywords: hyperspectral imaging, biomedical optics, biophotonics, digital histopathology, neurosurgery.

* Luca Giannoni (corresponding author), E-mail: giannoni@lens.unifi.it

† The authors contributed equally

1 Introduction

Histopathological screening of excised tissue is the current “gold standard” in post-surgical oncological practice¹, for clinical and molecular evaluation of critical parameters such as type, grading and classification of tumours, e.g., in glioma and glioblastoma (GBM) resection²⁻⁴. Normal routine involves the dispatch of fresh surgical biopsies after resection to the histopathology laboratory: there, the samples are typically fixed for preservation, sectioned, stained -various staining techniques are used, with haematoxylin and eosin (H&E) staining being the most prominent- and then imaged with a microscope to determine their structural and molecular composition³. However, modern histopathological analysis presents several limitations, the most severe one being the lengthy preparation of the samples that leads to long duration of the procedures to obtain the final results, which can vary from several days to even weeks after the surgery. Extemporaneous and intraoperative analyses can be much faster (minutes to hours), but the number of biopsy samples is limited due to operational logistics and costs of the procedures, and the breadth of information they can provide is very limited for diagnostic purposes⁵. Furthermore, diagnosis and classification can be affected by variability in the subjective interpretation of the results by histopathologists, with the screening essentially lacking a more quantitative and objective way to systematically process the imaging outcomes⁶. Overall, post-operative prognosis and planning would enormously benefit from a different approach to histopathology that could provide much faster and more reliable information on the tissue biopsies, ideally by having a screening *in situ* right after the surgery that could lead to quantitative results in a matter of minutes to hours.

Hyperspectral imaging (HSI) is an optical imaging modality that is becoming increasingly more notable in recent years in the biomedical and bioimaging fields⁷, and whose main features can be particularly suited and advantageous to tackle the abovementioned challenge. HSI acquires and

reconstructs images of a target at multiple, narrow, contiguous or adjacent wavelength bands in the electromagnetic spectrum, typically spanning from the visible to the near infrared (NIR) range⁸. This allows the user to obtain 3D spatio-spectral datasets, named “hypercubes”, where each spatial pixel of the images is associated with a corresponding spectrum of reflected, transmitted and/or fluorescent light. The information carried by the hypercubes is related to the optical properties of absorption and scattering of the investigated tissue, from which is then possible to infer, map and quantify its biochemical and structural composition, without the need for time-consuming staining procedures or the use of any exogenous contrast agent. Intrinsic biomarkers for physiology and pathophysiology of the tissue can indeed be identified for diagnostic purposes, such as haemoglobin for haemodynamics, oxygenation and vascularisation, or cytochrome-c-oxidase (CCO) for cellular metabolism⁸⁻¹⁰, and related to tumour key parameters of classification¹¹. In addition to its capabilities for non-destructive biochemical analysis of freshly excised tissue, HSI has the additional advantage of fast image acquisition and data processing, mainly thanks to recent advancements in deep learning and artificial intelligence (AI) algorithms¹², achieving near real-time computing and almost immediate visualization of the results¹³. Finally, HSI technology is typically compact and relatively inexpensive (compared to other traditional imaging modalities), so that devices can be developed to be fully transportable and capable to easily fit either within the surgical room or in its proximity (e.g., in a post-surgical area) without encumbrance.

We present here the first prototype of a compact, fully transportable HSI setup called “HyperProbe1”, which is able to rapidly select at high density, sampling and spectral resolution (3.5 to 7 nm of minimum bandwidth) any desired wavelength band between 510 and 900 nm, and to image a target at a field of view (FOV) of 0.9x0.9 mm² with up to 79 spectral bands, in less than 5 minutes. HyperProbe1 has the capability to image broadband reflected light from fresh biopsies

and to reconstruct maps of their optical properties, as well as to quantify the content of biomarkers of interest within the examined tissue (such as the two forms of haemoglobin and CCO) via fast spectral unmixing algorithms. We provide full technical characterisation of the performances of HyperProbe1 and a proof-of-concept of its application on samples of freshly excised glioma from surgical biopsies at different World Health Organization (WHO) gradings¹⁴. The success of HyperProbe1 in providing quantitative biochemical analysis and mapping of surgical biopsies can pave the way to a novel, fast and heightened methodology to perform *in situ* histopathological screening right after surgery, without the need for any manipulation or degradation of the samples.

2 Material and methods

2.1 The HyperProbe1 system

HyperProbe1 is a HSI system based on spectral scanning acquisition mode, where the target is illuminated in rapid sequence at each selected wavelength band, whilst a full-frame image is acquired synchronously at each illumination step.

Table 1 List of components of HyperProbe1 and their specifications.

Component	Manufacturer & model	Key specifics
SCL	NKT Photonics, SuperK FIANIUM FIR20	Broadband illumination (400-2400 nm); Maximum total power of 6.5 W;
AOTF	NKT Photonics, SELECT VIS-nIR	Broadband selection (510-900 nm); Spectral resolution of 3.5-7 nm (FWHM); 4.2-MP (2048 x 2048) CMOS sensor;
Camera	Hamamatsu, ORCA-Flash 3.0	6.5- μ m pixel size; QE up to 82% (Visible and NIR); Maximum frame rate of 40 fps;
Amplitude stabilisers	Thorlabs; NEL02A/M + NEL03A/M	Amplitude stabilisation within $\pm 0.05\%$;
Speckle reducer	Optotune; LSR-3005-6D-NIR	Transmission up to 98%;
Optic fibres	NKT Photonics, SuperK CONNECT	Broadband coverage (400-2000 nm); High power throughput (up to 500 mW); 1-mm core diameter;
Objective	Thorlabs, LMM15X-P01	15x reflective objective; NA = 0.3;

CMOS: Complementary metal-oxide semiconductor; FWHM = Full-width at half maximum; QE = Quantum efficiency; NIR = Near-infrared; FOV = Field of view; NA = Numerical aperture.

All the spectral frames are then stacked together to reconstruct the corresponding 3D hypercube of the target⁸. A schematic of the configuration of HyperProbe is reported in Fig.1a, whereas a detailed list of its components is presented in Table 1.

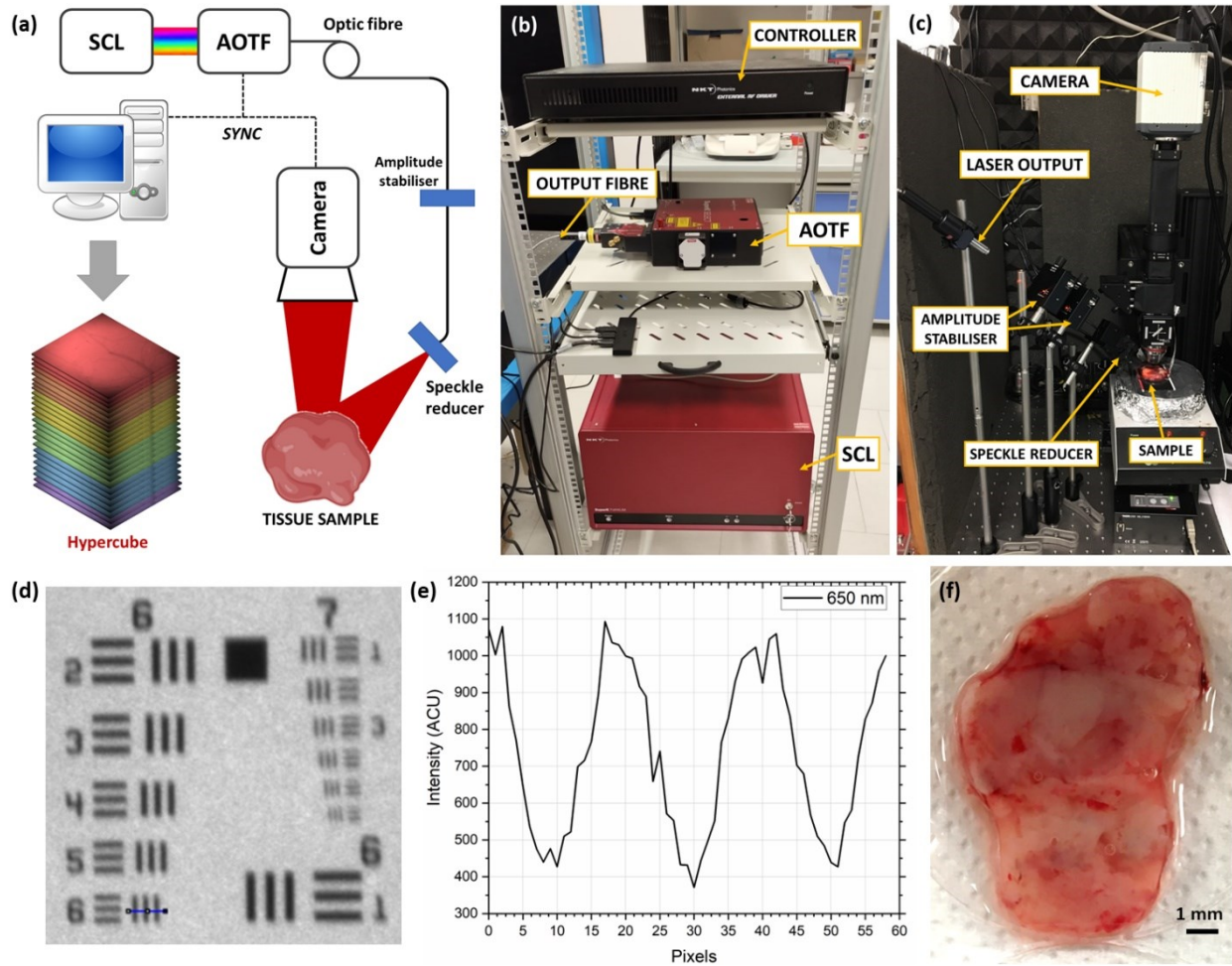


Fig. 1 (a) Schematics of the HyperProbe1 with all its components; (b) Picture of the spectral illumination side of HyperProbe1, including the SCL source, the AOTF and the controlling devices; (c) Picture of the imaging and detection side of HyperProbe1, depicting the illumination output, the amplitude stabilisers, the speckle reducer and the camera; (d) Result of the imaging tests on the USAF1951 target with HyperProbe1 at 650 nm; (e) The smallest resolved line pair (group 6, element 6) highlighted in blue and its corresponding line profile that shows minimum FWHM separation ($4.38 \mu\text{m}$); (f) Example of a sample of excised glioma tissue obtained from the surgical biopsies.

The illumination side of HyperProbe1 (Fig. 1b) is composed of a supercontinuum laser¹⁵ (SCL;

NKT Photonics, SuperK FIANIUM FIR20), generating a coherent, broadband illumination (400-2400 nm) at a maximum total power of 6.5 W, and a set of acousto-optic tuneable filters (AOTF; NKT Photonics, SELECT VIS-nIR) that selectively filters any desired spectral band between 510 and 900 nm, with a minimum bandwidth (full width at half maximum; FWHM) of 3.5 nm in the visible and a maximum bandwidth of 7 nm in the NIR range. The filtered light from the AOTF is directed to the sample through an optic fibre delivery system (NKT Photonics, SuperK CONNECT) of 1-mm core diameter, coupled with: (1) a pair of laser amplitude stabiliser connected in series (Thorlabs, NEL02A/M and NEL03A/M), to eliminate intensity noise and maintain illumination stability over time within 0.05% of a selected output power across the whole spectral range, (2) a laser speckle reducer (Optotune, LSR-3005-6D-NIR), and (3) an achromatic doublet lens, to make the beam divergent in order to obtain an illumination spot of 2-3 cm² on the target. Image acquisition at each spectral band is obtained on the imaging side of HyperProbe1 (Fig. 1c) by use of a complementary metal-oxide semiconductor (CMOS) camera (Hamamatsu, ORCA-Flash 3.0). The CMOS camera has a sensor size of 2048 x 2048 pixels, with pixel size of 6.5 μm, 82% peak quantum efficiency (at 620 nm), and maximum readout rate of 40 fps. It is coupled with a 15x reflective objective (Thorlabs, LMM-15X-P01) and an infinity-corrected, conjugated tube lens (Thorlabs, TTL200-B), to generate a FOV of the target of about 0.9 x 0.9 mm². The whole setup is mounted on a wheeled rack (as depicted in Fig.1b) and can be easily transported within or adjacent to the surgical room, with the illumination probe and imaging side that can be laid on a small breadboard for improved stability.

The HyperProbe1 system was characterised in terms of power emission, spectral, temporal and imaging performances. The complete characteristics and features of HyperProbe1 are reported in Table 2. HyperProbe1 can scan the entire spectral range of operation (510-900 nm) by sampling

sequentially up to 79 wavelength bands at 5-nm steps. Each spectral band is also modulated in amplitude by the AOTF, to provide an approximately constant output power on the target of about 200-450 μW per band, accounting also for the quantum efficiency (QE) of the camera. This is aimed at maintaining a fixed integration time of the camera for each spectral frame (between 5 and 30 ms, depending on the target), as well as an adequate signal-to-noise ratio (SNR) throughout every acquired spectral frame. The typical acquisition time for an entire hypercube (79 bands) ranges between 1 to 5 minutes (depending on the selected integration time of the camera), for biological targets. Spatial resolution of HyperProbe1 was assessed for each single spectral band via imaging of a positive resolution test target, the USAF 1951 (Thorlabs, R1L1S1P). For all these imaging assessments, the spatial resolution of HyperProbe1 was found equal to 114 lp/mm, corresponding to a smallest resolvable detail of 4.38 μm (as shown in Fig. 1d and Fig. 1e, for 650 nm).

Table 2 Technical characteristics and features of HyperProbe1.

Characteristics	Illumination side
Illumination mode:	Spectral scanning
Available spectral range:	510-900 nm
Minimum sampling step size:	5 nm
Maximum number of spectral bands:	79 (visible and NIR)
Spectral resolution (FWHM):	3.5 nm (visible), 7 nm (NIR)
Average output power per spectral band:	$\sim 200 \mu\text{W}$ (visible), $\sim 450 \mu\text{W}$ (NIR)
Power stability over time:	$\pm 0.05\%$
Characteristics	Imaging side
Type of detector:	CMOS
Sensor format:	2048 x 2048 pixels
Pixel size:	6.5 μm
Spatial resolution:	4.38 μm
FOV:	0.9 x 0.9 mm^2
Frame rate:	40 fps (at full format)
Sensitivity (QE):	82% at 620 nm
Typical acquisition time (per spectral frame):	5 to 30 ms
Typical acquisition time (per hypercube):	1 to 5 min

NIR = Near-infrared; FWHM = Full-width at half maximum; CMOS: Complementary metal-oxide semiconductor; FOV = Field of view; QE = Quantum efficiency.

2.2 Samples preparation and data acquisition

HyperProbe1 was used to image a series of fresh surgical biopsies of glioma tissue, to validate its performances in retrieving quantitative information of interest on the composition of samples, as well as to infer pathological characteristics of the tumours akin to what is obtained via traditional histopathological screening. The brain tissue samples involved in the study (an example is shown in Fig. 1f) were obtained from fresh surgical excisions of patients taken during routinely performed neurosurgery for brain tumour resection at the Azienda Ospedaliero-Universitaria Careggi (University Hospital of Florence), in Florence. Authorization for the study (Studio ID: 23672 - 23672_BIO) was granted by the Ethical Committee of the Area Vasta Centro Toscana, under Italian law and regulations. Informed consent was collected from each patient involved in the study.

A total number of 11 samples ($n = 11$) were imaged and analysed with HyperProbe1, to guarantee a degree of statistical robustness in the reconstructed spectra and to investigate specimen variability. The samples were composed of portions of the same tissue removed during the resection that is normally sent to the laboratory for histopathological screening, which classified the type of the tumour based on WHO gradings¹⁴. This class of information for all the samples is reported in Table 3, providing a broad characterisation of various typologies of glioma.

Table 3 Classification of the tissue samples investigated with HyperProbe1.

Sample identifier	WHO grading	Additional info
S1	IV	
S2	IV	
S3	III	Discarded due to fragmented size
S4 (FOV1)	IV	Two separate FOVs were acquired on the same sample
S4 (FOV2)	IV	Two separate FOVs were acquired on the same sample
S5	IV	Labelled with fluorescein
S6	II	Discarded due to presence of light interference
S7	II	Possibly shifting to higher grade (III)
S8	III	Labelled with fluorescein, presence of coagulated tissue
S9	IV	Labelled with fluorescein, but negative
S10	II	Labelled with fluorescein
S11	IV	Labelled with fluorescein, but negative

FOV = Field of view.

Two samples were discarded from the analysis: sample S3 was a biopsy composed of very small and dispersed fragments of brain tissue (2-3 mm each at most) and, due to their dimensions, the acquired spectra appeared very flat (we hypothesise a large influence of partial volume effect); conversely, sample S6 presented ambiguous patterns due to potential light interference at some wavelengths. In addition, for sample S4, due to its slightly larger dimensions than the rest of the biopsies (5-6 cm), it was decided to acquire two separate FOVs on the same tissue to further analyse variability within subjects. Finally, samples S8, S9, S10 and S11 were marked with fluorescein during the surgery, albeit S9 and S11 were confirmed to be negative to fluorescent emission.

For the HSI data acquisition, a portion of the glioma samples (average size of 2-3 cm) was preemptively washed in phosphate-buffered saline (PBS) to eliminate blood and other unwanted residuals, then imaged on its surface with HyperProbe1 (79 wavelength bands at 5-nm steps between 510 and 900 nm) within 1 hour after excision. A thin glass coverslip was placed over each sample to flatten its top surface for uniform focusing of the FOV, whilst a dark absorbing material was placed at the bottom to avoid any potential reflection of the light back into the tissue. The acquisition of a single hypercube for every sample was typically less than 5 minutes, a short enough duration to ensure that the tissue had not deteriorated nor oxidised during the imaging.

2.2 Data processing and spectral unmixing analysis

Reflectance hypercubes $R(x, y, \lambda)$ for each sample were reconstructed by normalising the hyperspectral data of the reflected light intensity $I(x, y, \lambda)$ acquired with HyperProbe1 with reference hypercubes $W(x, y, \lambda)$ obtained using a white calibration standard (Labsphere, Spectralon® 5"), after dark counts subtraction $D(x, y, \lambda)$, and by weighting the latter two datasets for the ratios of their corresponding integration times t of the camera used during the acquisition. The formula for the reconstruction of the reflectance hypercubes is

$$R(x, y, \lambda) = \frac{I(x, y, \lambda) - \frac{t_I}{t_D} D(x, y, \lambda)}{\frac{t_I}{t_W} W(x, y, \lambda) - \frac{t_I}{t_D} D(x, y, \lambda)} \quad (1)$$

where t_I , t_D and t_W are the camera integration times for each frame of the intensity, dark and white hypercubes, respectively.

A fast, spectral unmixing approach based on modified Beer-Lambert's law (MBLL) was used to infer the differences in the molecular composition of the biopsies, as described in Ezhov *et al*¹⁶. These differences were quantified with respect to sample S1, using the average spectral reflectance of the central area of the sample as baseline spectrum. Computational time to analyse a full dataset from each biopsy was about 2-3 minutes with two AMD EPYC 7452 32-Core processors.

We then compared the inferred compositions for two different scenarios: (1) by fitting the whole measured wavelength range (from 510 nm to 900 nm), and (2) by fitting only the NIR portion of the available spectrum (in our case, from 740 nm to 900 nm). For the latter, we expected the major absorbing chromophores to be oxygenated (HbO₂) and deoxygenated (HHb) haemoglobin, the oxidised (oxCCO) and reduced (redCCO) forms of cytochrome-c-oxidase (CCO), as well as water and lipids^{8,17,18}. The spectral signatures of the chromophores targeted by the analysis are depicted in Fig. 2a and Fig. 2b. In the visible range, we also assumed the presence of additional chromophores, specifically the oxidised and reduced forms of cytochrome-b (Cyt-B) and cytochrome-c (Cyt-C), due to their involvement in the metabolic processes¹⁷.

The inferred compositions, in the forms of either concentrations or volumetric contents, are in units [mM/cm] and [cm⁻¹], respectively, as we used unitary pathlength (1 cm) in our experiments. We have previously seen that a quasi-constant pathlength only effectively scales the concentrations, at least in the NIR range¹⁶, and is therefore sufficient for the preliminary task of attempting to distinguishing biopsies of different tumour gradings.

2.3 Monte Carlo simulations of penetration depth in tissue

A 3D, *in silico*, optical and geometrical model of brain biopsy was designed to assess and quantify the depth of penetration of light in the tissue, at the various spectral bands of HyperProbe1⁹. This was done in MATLAB using a voxel-based Monte Carlo (MC) simulation software. The software chosen was Monte Carlo eXtreme (MCXLAB)^{20,21}, which simulates photon transport within a 3D, voxel-based model with arbitrary optical properties. The simulations were carried out on a desktop computer with an Intel Xeon W5-3425 and two RTX 4090 GPUs.

The simulated geometry consisted of a homogeneous, semi-infinite slab of grey matter with a thickness of 0.5 cm (taking into account the maximum thickness recorded among the investigated samples). Isotropic voxels were used, with dimensions of 0.05 mm. This was chosen as it offered an acceptable trade-off between accuracy and computational performances. A black absorbing layer of 0.005-cm thickness with a significantly higher absorption coefficient (in the order of 10^6 cm^{-1}) was placed at the bottom of the slab, to represent the absorbing material used below the biopsies. Fresnel reflection was implemented at the top and bottom boundaries of the model²⁰.

The reduced scattering coefficient μ'_s of the grey matter of the model was adopted from Jacques *et al*¹⁸, and was varied with wavelength according to the following equation:

$$\mu'_s = a \left(\frac{500 \text{ nm}}{\lambda} \right)^{-b}, \quad (2)$$

where $a = 40.8 \text{ cm}^{-1}$, and $b = 3.089$. From μ'_s , the scattering coefficient μ_s was calculated as an input for MCXLAB with the equation:

$$\mu_s = \frac{\mu'_s}{1 - g}, \quad (3)$$

where g is the anisotropy factor of grey matter standing at 0.85 and chosen to be constant, as its variation with wavelength has been demonstrated to be minimal for cerebral tissue²². Furthermore,

the refractive index of the biopsy model was set to 1.36¹⁸.

Finally, the 3D model of brain biopsy was assumed to be composed of the most absorbing and scattering tissue chromophores, i.e., water, lipids, HbO₂, HHb, oxCCO and redCCO⁹. Thus, the total absorption coefficient μ_a of the model was determined using the equation^{9,18}:

$$\begin{aligned} \mu_a = & W \cdot \mu_{a,H_2O} + F \cdot \mu_{a,fat} + \ln 10 \cdot C_{HHb} \cdot \varepsilon_{HHb} + \ln 10 \cdot C_{HbO_2} \cdot \varepsilon_{HbO_2} + \\ & + \ln 10 \cdot C_{oxCCO} \cdot \varepsilon_{oxCCO} + \ln 10 \cdot C_{redCCO} \cdot \varepsilon_{redCCO}, \end{aligned} \quad (4)$$

where W and F are the water and lipids volumetric contents, respectively; μ_{a,H_2O} and $\mu_{a,fat}$ are the absorption coefficients of water and lipid, respectively; C_{HHb} , C_{HbO_2} , C_{oxCCO} , and C_{redCCO} are the molar concentrations of HHb, HbO₂, oxCCO and redCCO, respectively; and ε_{HHb} , ε_{HbO_2} , ε_{oxCCO} and ε_{redCCO} are the molar extinction coefficients of HHb, HbO₂, oxCCO and redCCO, respectively. W , F , C_{HHb} , C_{HbO_2} , C_{oxCCO} , and C_{redCCO} are derived from Giannoni *et al*⁹, whereas the absorption coefficients μ_{a,H_2O} and $\mu_{a,fat}$ (graphed in Fig. 2a), as well as the molar extinction coefficients ε_{HHb} , ε_{HbO_2} , ε_{oxCCO} and ε_{redCCO} (graphed in Fig. 2b) were derived from Giannoni *et al*⁹ and Prahl *et al*¹⁹. Table 4 summarises the main composition of the 3D *in silico* model of brain biopsy used for the MC simulations, based on human grey matter.

Table 4 Composition of the 3D *in silico* model of brain biopsy used for the MC simulations.

Model composition	Values
Water content, W	70%
Lipid content, F	10%
Molar concentration of HHb, C_{HHb}	56.7 μ M
Molar concentration of HbO ₂ , C_{HbO_2}	56.7 μ M
Molar concentration of oxCCO, C_{oxCCO}	1 μ M
Molar concentration of redCCO, C_{redCCO}	4 μ M

HHb = Deoxygenated haemoglobin; HbO₂ = Oxygenated haemoglobin; oxCCO = oxidised cytochrome-c-oxidase; redCCO = reduced cytochrome-c-oxidase.

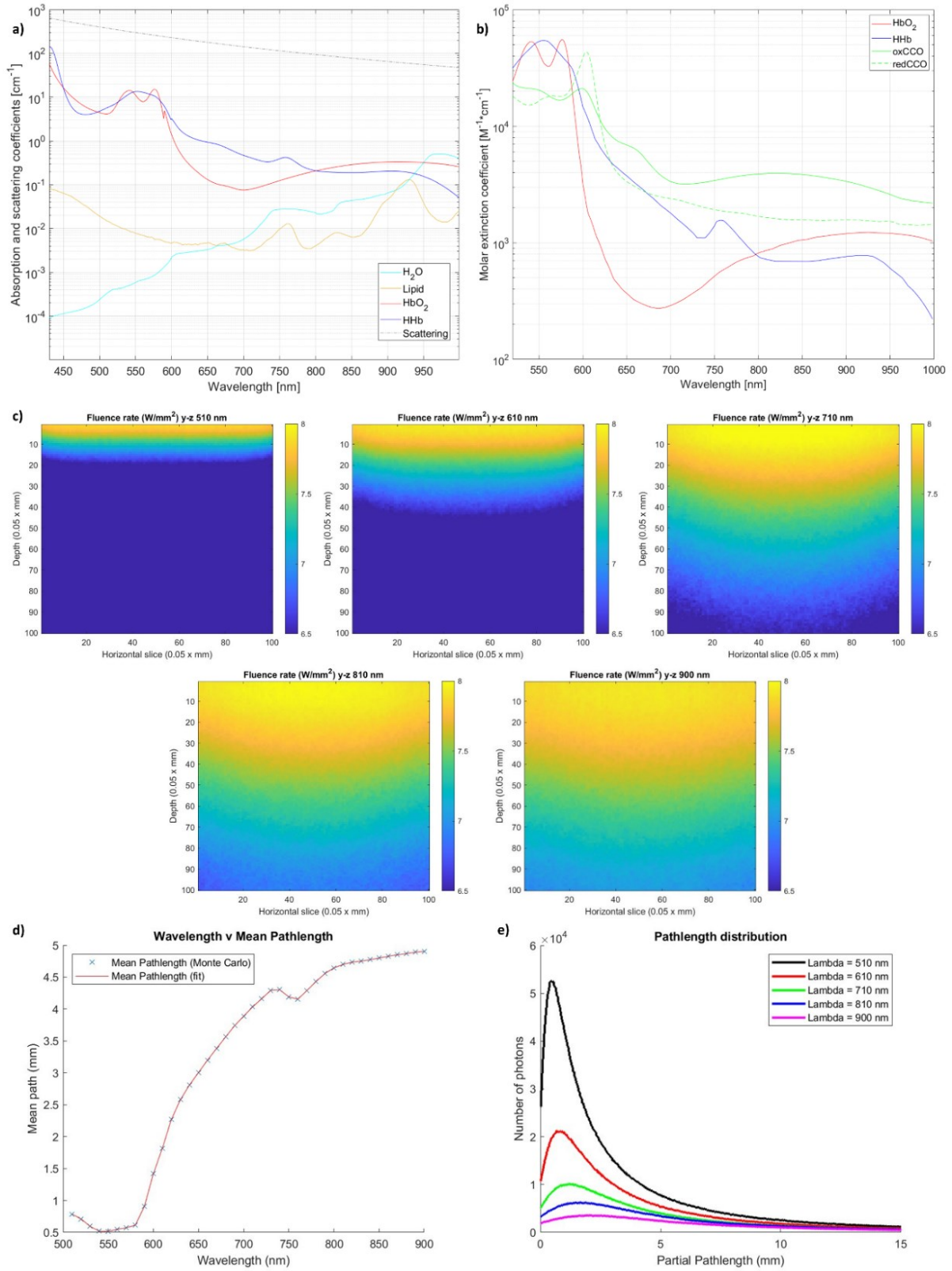


Fig. 2 (a) Absorption coefficients for HbO_2 , Hb, lipids and water, and scattering coefficient of generic brain tissue in the visible and NIR range (150 g/L concentration of Hb in blood and blood volume content in generic brain tissue

equal to 5% are assumed)^{8,19}; b) Molar extinction coefficients of HbO₂, HHb, oxCCO and redCCO in the visible and NIR range^{8,17}; c) Simulated fluence rates within the 3D cerebral biopsy model at different wavelengths (the plots are in a logarithmic scale and the absorbing layer was excluded from the plots to maintain a visible contrast). The distribution of the fluence showed a noticeably higher penetration of the light at the NIR wavelengths; d) Simulated mean photon pathlength within the 3D biopsy model, as a function of wavelength; e) Partial pathlength distributions of the photons simulated within the 3D biopsy model at various wavelengths (as previously, the absorbing layer was not included in this figure due to a negligible number of photons passing through it).

A planar, divergent light source was positioned above the 3D biopsy model to simulate the illumination of the grey matter slab at the same wavelengths of operation of the HyperProbe1 (500-900 nm, at 5-nm sampling). The direction of the illumination was normal the z axis. A total of 10^7 photons were simulated for each wavelength band, with emission power equal to 1 mW.

Simulated fluence rates for each wavelength were obtained from the MC simulations, allowing to visualise and assess the spatial distribution of the photons at the different spectral bands within the 3D model. Examples of these distributions are depicted in Fig. 2c, demonstrating increasing depth of penetration of the light within the tissue for longer and longer wavelengths. The depth of penetration of the photons in the model of biopsy ranged from 10-15% of its thickness (about 0.5-0.75 mm) for the visible light, up to almost the whole size of the sample (5 mm), for the NIR light.

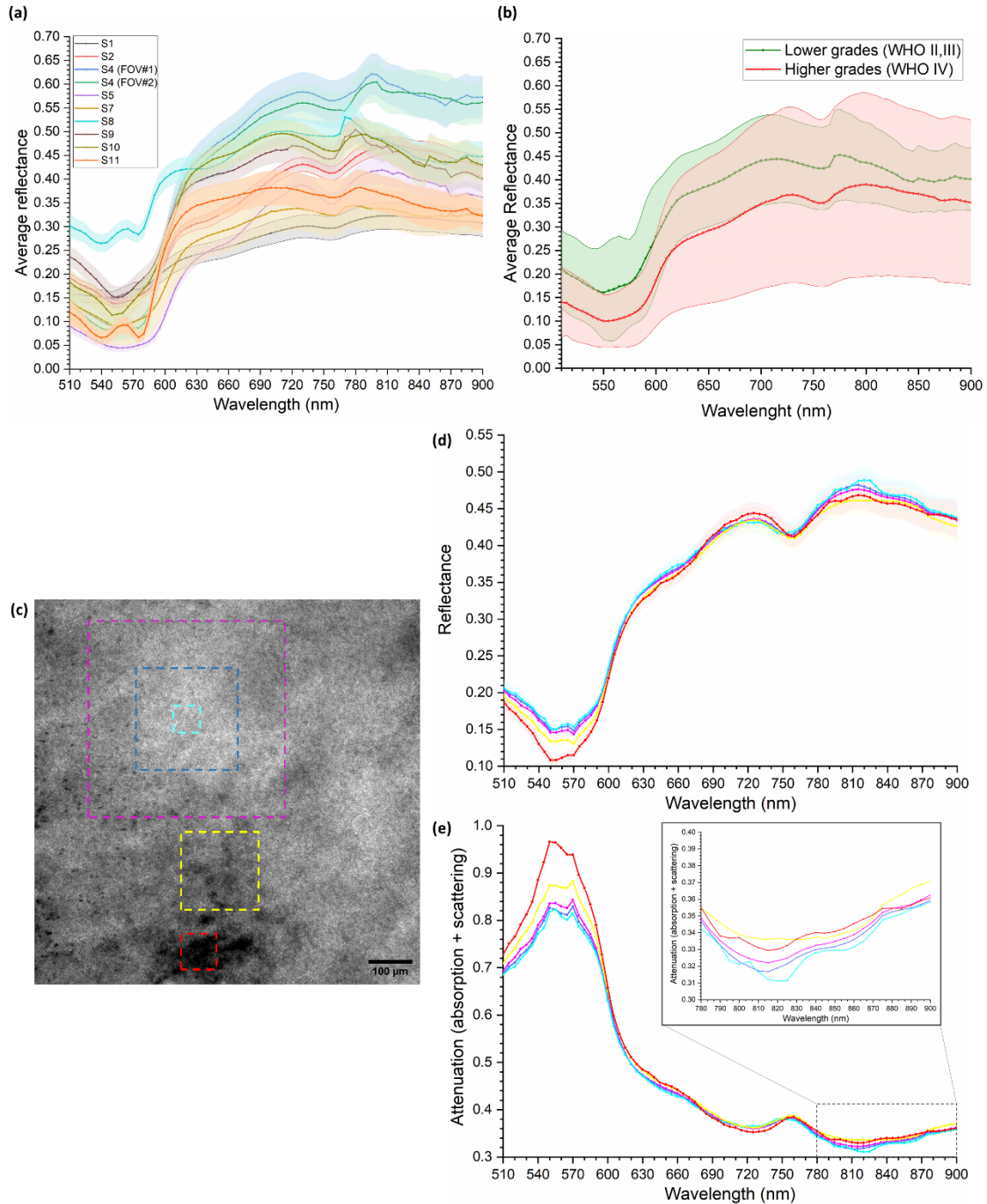
To further investigate the relationship between wavelength and penetration depth of the light, the mean pathlength across the tissue of the simulated photons was estimated from the MC simulations for each spectral band, as reported in Fig. 2d. The results further demonstrate that the mean pathlength travelled by the photon within the tissue increases as the wavelength of the light gets longer, up to about 5 mm (at 900 nm). Nonetheless, this gradual increase is not homogeneously continuous, as local extrema are identifiable in Fig 2c, corresponding to the peaks of absorption of haemoglobin at about 530-570 nm and 770 nm (as visible in Fig. 2a).

Finally, distributions of the partial pathlengths of the simulated photons were estimated for each wavelength of HyperProbe1: Fig. 2e depicts examples of these distributions across the full range of the system (the absorbing layer at the bottom is excluded). The results, together with the outcomes previously illustrated, demonstrate empirically that HyperProbe1 does not simply map the optical properties of the investigated tissue on its visible surface, but actually reconstruct an integrated distribution on 2D of the spectral features of the biopsy samples across their entire 3D volume, thanks to the use of both visible and NIR light with different penetration capabilities.

3 Results

3.1 Qualitative and comparative evaluation of the HyperProbe1 data

Preliminary qualitative evaluation of the data collected with HyperProbe1 on the cerebral *ex vivo* tissue was conducted, to assess both heterogeneity in the spectra within the same sample, as well as spectral variability between all the biopsies. For intercomparison across the various samples described in Table 3, each processed reflectance hypercube $R(x, y, \lambda)_n$, for $n = S1 \dots S11$, was averaged spatially over its entire FOV, in order to obtain a single averaged reflectance spectrum for each biopsies. All these reflectance spectra are shown altogether in Fig. 3a. Overall, the average reflectance spectra between samples share similar trends, reporting low reflectance in the visible range (where absorption from haemoglobin is at its highest, as per Fig. 2a), which then tends to increase gradually towards the NIR range beyond 600 nm, where scattering becomes predominant. However, significant variability in both magnitudes of the spectra in the same regions and in their local features are also present, differentiating the signatures of the various samples. Such aspect is further highlighted by averaging the abovementioned spectra according to their WHO grading: lower grade glioma (LGG) samples (WHO grade II and III) were grouped together and the mean



1 **Fig. 3** (a) Intercomparison of averaged reflectance spectra over the entire imaged FOVs of each biopsy sample;
2 (b) Comparison between average reflectance spectra grouping LGG (WHO II, III) against HGG samples (WHO IV);
3 (c) Processed spectral image from HyperProbe1, at 560 nm, of HGG (WHO grade IV) biopsy sample S2, with high-
4 lighted, selected ROIs in the FOV in which average reflectance spectra were calculated; (d) Example of average re-
5 flectance spectra in the corresponding ROIs of the biopsy sample S2; (e) Example of average attenuation spectra in
6 different ROIs of biopsy sample S2, with the portion within the NIR range 780-900 nm enlarged.

7 of their average reflectance spectra across the whole FOVs was compared against the same mean
8 for all the higher grade glioma (HGG) samples (WHO grade IV), as reported in Fig. 3b. It can be
9 seen that there are indeed significant differences in the means between LGG and HGG samples,
10 regarding both local spectral trends as well as magnitude, with the LGG mean presenting higher
11 reflectance on average along the entire spectral range. Conversely, HGG shows larger variance
12 among biopsies of their corresponding group, for the same grade.

13 A number of different regions of interest (ROI) were selected on the reflectance hypercubes
14 $R(x, y, \lambda)$ to calculate average reflectance spectra, including different sizes and portions of the
15 FOV reporting identifiable visual features, such as blood clusters. This was done to investigate
16 potential spatial changes in the reflectance spectra across the FOV of the samples. Fig. 3c shows
17 an example of a single, processed reflectance spectral image (as described in Sec. 2.2) collected
18 with HyperProbe1 for arbitrary HGG (WHO grade IV) sample S2, at the bandwidth centred at 560
19 nm, whereas Fig. 3d depicts the corresponding average reflectance spectra. The comparison of the
20 reflectance spectra for each sample on different ROIs highlights significant (from 0.0017 to 0.0378
21 average root mean square deviation (RSMD) for the reflectance curves across all samples) differ-
22 ences in their shapes and trends, as visible for the model case of S2 in Fig. 3d, for two specific
23 spectral ranges: (1) between 510 and 660 nm, and (2) between 780 and 880 nm. In contrast, outside
24 of these ranges, the remainder of the spectral signatures displays homogeneous distribution of the
25 optical properties of the *ex vivo* samples across the entire FOVs. The largest differences (0.0378
26 of average RSMD across samples) are reported for the ROIs where accumulation of blood are
27 clearly visible. For the first mentioned range (510-600 nm), such results could be correlated to the
28 presence and strong influence of the visible peaks of haemoglobin absorption (Fig. 2a). The influ-
29 ence of the absorption of haemoglobin could also be connected to the reported differences in the

30 spectra for the second mentioned range (780-880 nm), which is characterised by a broad peak of
31 absorption from HbO₂. However, differences are identified in the biopsy samples also for ROIs
32 not including visible blood clusters: this could then be connected to local differences in the con-
33 centrations of CCO, as the identified range overlaps with the NIR absorption peak of the latter
34 (Fig. 2b), as well as for the increasing weight of the absorption of water and lipids towards the end
35 of the NIR range (Fig. 2a).

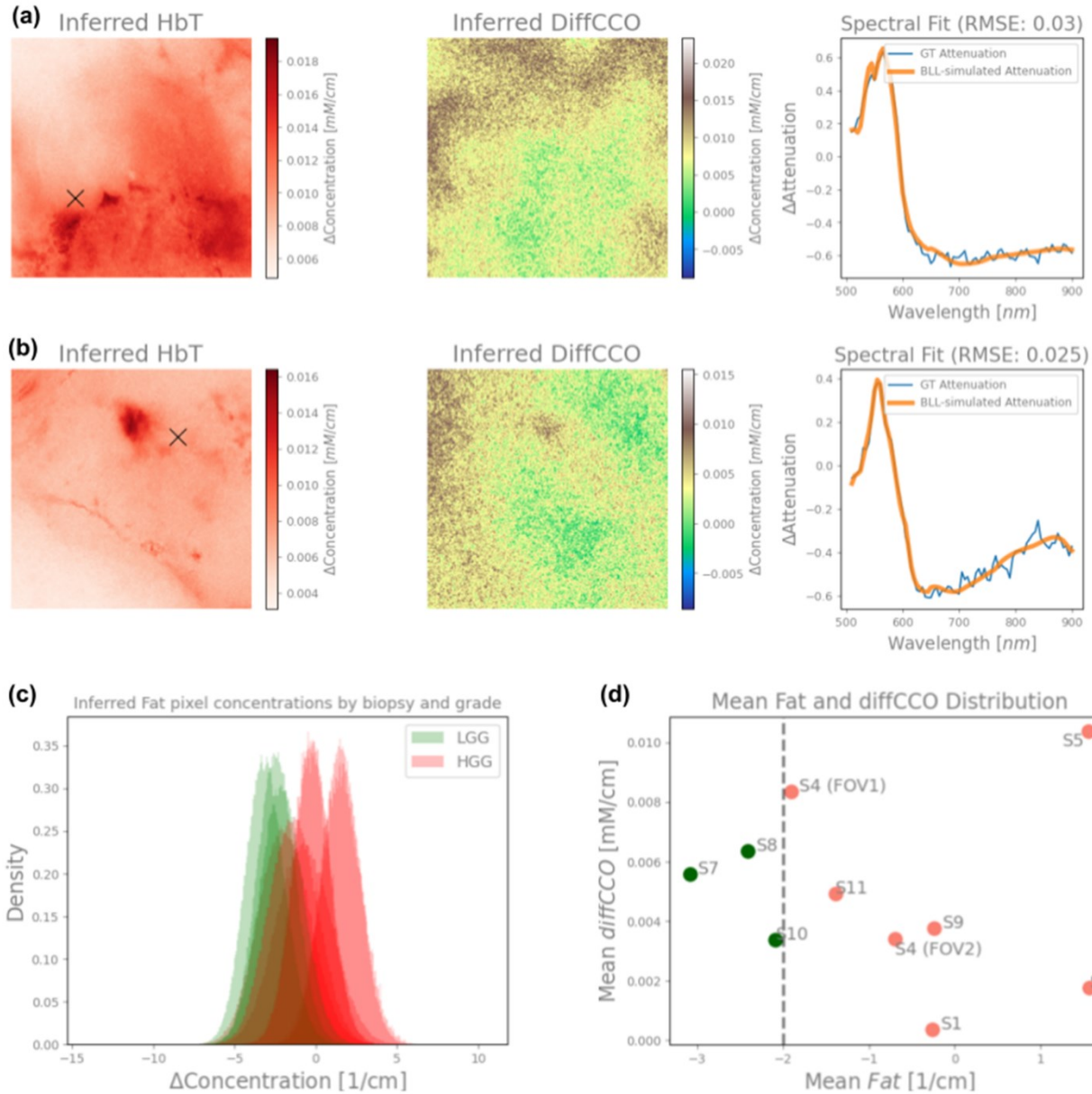
36 For a more direct comparison between the spectral signatures of the biopsies reconstructed with
37 HyperProbel and the pure optical signatures of the chromophores of interest reported in Fig. 2a
38 and Fig. 2b, we calculated the attenuation spectra $A(x, y, \lambda)$ associated with the contribution of
39 optical absorption and scattering in the tissues, from the reflectance spectra $R(x, y, \lambda)$ in the same
40 ROIs of the samples, using the formula: $A(x, y, \lambda) = -\log_{10}(R(x, y, \lambda))$. Fig. 3e reports, for in-
41 stance, the average attenuation spectra of the same HGG sample S2 and the previously selected
42 ROIs. In the range 510-600 nm, the attenuation spectra of the brain tissue samples correlate with
43 the combined profiles of the absorption spectra of HbO₂ and HHb, with noticeable peaks at around
44 545-555 nm and at 575 nm. Another peak is also identified in all samples at around 755-760 nm,
45 overlapping the equivalent one from the absorption spectra of HHb. In all samples, attenuation in
46 the range 510-600 nm is reported to increase gradually when shifting from ROIs with no visible
47 accumulations of blood towards ROIs that include the latter at different degrees of covering (as
48 visible for the case of S2 in Fig. 3d). Figure 3e highlights and enhances the visualisation of the
49 attenuation spectra from S2 in the range between 780 and 900 nm, where differences are reported
50 for all the ROIs regardless of the presence of any discernible spatial feature or difference in con-
51 trast. This is occurring largely across all the analysed samples of surgical biopsies. In particular,
52 localised peaks of attenuation corresponding to about 840 nm are identified in a number of ROIs

53 in the samples, where the optical absorption of oxCCO is also at its highest. The reported discrep-
54 ancies among concentric ROIs of different sizes in relatively homogenous areas of the *ex vivo*
55 tissue could be linked to either local variation in the abovementioned chromophore, as suggested
56 by the overlapping of the peaks, or to partial volume effects connected to changes in the optical
57 pathlength travelled by the lights within the sampled regions⁹.

58 3.2 *Quantitative biochemical analysis of the HyperProbel data with spectral unmixing*

59 As mentioned in Sec. 2.2, we compared the inferred compositions of the expected chromophores
60 from the spectral unmixing algorithm in all the biopsy sample, for two different fitting scenarios:
61 in the whole range from 510 nm to 900 nm, and in the NIR portion of the spectrum from 740 nm
62 to 900 nm. For the first scenario, we obtained satisfactory spectral fits matching the measured
63 attenuation: an example is depicted in Fig. 4a and Fig. 4b, for HGG sample S4 in FOV#1 (WHO
64 grade IV) and LGG sample S10 (WHO grade II), showing also the reconstructed quantitative maps
65 for the total concentration of haemoglobin (HbT), given as the sum of HbO₂ and HHb, as well as
66 for the concentration of differential CCO (diffCCO), given as the difference between the concen-
67 trations of oxCCO and redCCO^{8,17}. Blood clusters are resolved with high resolution, due to the
68 haemoglobin peaks in the 500-600 nm range and the expected high concentration and absorbance
69 of haemoglobin (compared to the other known chromophores). Similar well-matching spectral fits
70 via the MBLL are found across all patients, as we report the root mean square error (RMSE) means
71 across all pixels and across all patients to be in the range 0.017 to 0.039, which is of similar mag-
72 nitude to the exemplary RMSEs reported in Fig. 4.

73 A preliminary attempt to classification of the biopsy samples from the inferred hyperspectral
74 results was also performed. As shown in Fig. 4c and Fig. 4d, we found that predicted lipids content
75 allows to separate LGG (grade II and III) biopsies from HGG biopsies (grade IV). Even though

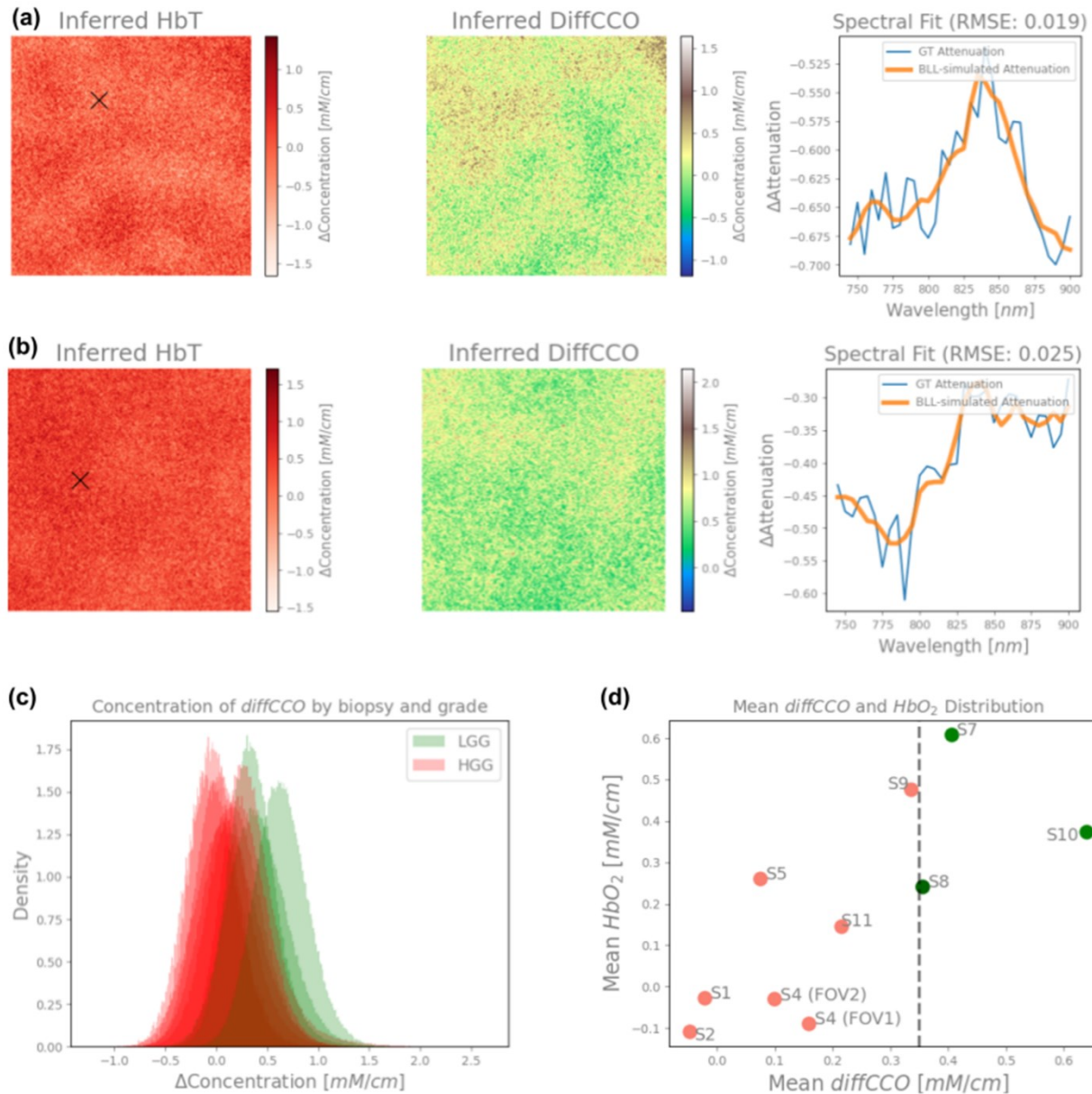


77 **Fig. 4** Inferred HbT and diffCCO concentration maps of HGG S4 FOV#1 (a) and LGG grade S10 (b) samples fitting
 78 the whole measured wavelength spectrum (510-900 nm), whilst a model fitting of the observed attenuation for the
 79 marked pixel in the HbT image is shown in the third column for both biopsies; (c) Histogram showing probability
 80 density distribution of inferred lipid volumetric content of each pixel across different LGG (displayed in green) and
 81 HGG (displayed in red) grade samples; (d) Distribution means of the lipid content (reported on x-axis) and diffCCO
 82 concentrations (reported on y-axis) suggest that lipid mean content could be able to distinguish grading of all sam-
 83 ples, whereas no apparent separation is visible for the inferred mean diffCCO concentrations.

84

85 we observe significant overlap between the different distributions (with an overlap coefficient of
86 49.96% assuming normal distributions), we generally noticed a trend of higher differential lipids
87 content in HGG biopsies, with a mean of -0.466 cm^{-1} . Conversely, the LGG samples were found
88 to have a mean lipid content of -2.53 cm^{-1} . The distinction between the two gradings for all samples
89 was possible by computing the means across all the biopsies and using the -2 cm^{-1} lipid content
90 difference threshold, as shown in Fig. 4d. This difference in means of the tumour grades was also
91 found to be statistically significant via the Mann-Whitney U test ($p=0.017$), testing for equal
92 means. Conversely, we did not find evidences of CCO or haemoglobin (established biomarkers
93 for cellular metabolism and haemodynamics, respectively⁸) to be able to separate gradings of gli-
94 oma samples in the whole range 510-900 nm (as it can be seen in Fig. 4d, for CCO). The overlap
95 coefficient between LGG and HGG samples was found to be considerably larger, with 81.2% and
96 84.6% for inferred diffCCO and HbO_2 concentrations, and statistical differences in grading were
97 not observed ($p=0.84$ and $p=0.99$, respectively). On a final note, as seen on Fig. 4d, by considering
98 both variables (lipid content and diffCCO concentration) on the 2D distribution plot, an oblique
99 line could arguably even better separate the two glioma grades. A larger sample size will be re-
100 quired to test such more complex hypotheses further.

101 In the second scenario, we estimated inferred compositions within the biopsy samples using
102 exclusively the NIR range between 740 nm and 900 nm, which was chosen to target chromophores
103 that are known for their characteristic absorption profiles in such range, particularly oxCCO and
104 redCCO (as seen in Fig. 2b). Indeed, MBLL has been commonly employed in this specific NIR
105 range to infer differences in metabolic activity using CCO as a biomarker^{8-10,17}. As shown in Fig.5a
106 and Fig. 5b, we again fit the observed signal qualitatively well: the inter-biopsy mean RMSE errors
107 are found to be in the range 0.0151 to 0.296, i.e., the spectral fits of all biopsies can be expected
108



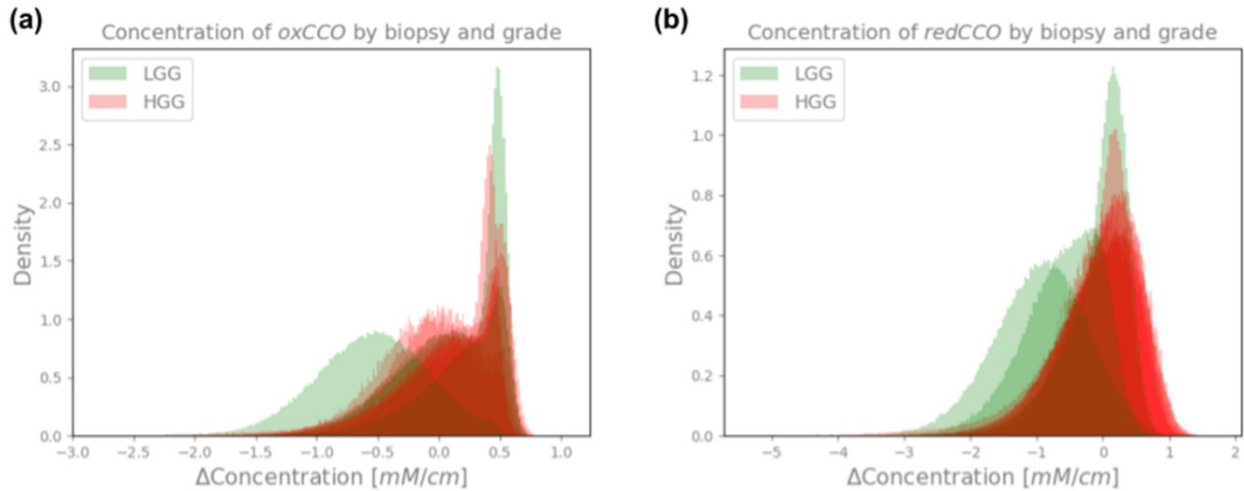
109 **Fig. 5** Inferred HbT and diffCCO concentration maps of HGG S4 FOV#1 (a) and LGG S10 (b) samples fitting ex-
 110 clusively the NIR range (740-900 nm), whilst a model fitting of the observed attenuation for the marked pixel in the
 111 HbT image is shown in the third column for both biopsies; (c) Histogram showing probability density distribution of
 112 inferred diffCCO concentrations of each pixel across different LGG (displayed in green) and HGG (displayed in
 113 red) grade samples; (d) Distribution means of diffCCO and HbO₂ concentrations suggest that these parameters could
 114 be able together to distinguish lower and higher grade samples of glioma tissue, with diffCCO being the most accu-
 115 rate, across all the investigated samples.

116

117 to be similar as observed in Fig.5a and Fig. 5b, as for the previous scenario, albeit being slightly
118 worse due to the expected reduction in SNR at the latter end of the measured spectrum, where
119 scattering of light become predominant. Notable loss in the resolution of various blood clusters
120 can be observed, which was also expected due to the exclusion of the 510-600 nm range with larger
121 haemoglobin absorption peaks. Interestingly, we observed significant differences to the inferred
122 molecular concentrations across biopsies of LGG and HGG that do not match the ones highlighted
123 by the spectral analysis on the whole wavelength range: e.g., in this scenario, the inferred lipid
124 contents were not able to distinguish between the different grades of the samples. We reported an
125 overlap coefficient of 77.1% and no statistical differences in the concentration means for lipids in
126 this scenario ($p=0.84$). However, we observed average concentrations differences of metabolic
127 diffCCO between LGG and HGG samples, with HGG samples showing lower diffCCO mean con-
128 centrations, as seen in Fig. 5c and Fig. 5d. The diffCCO concentration threshold at 0.35 mM/cm
129 was able to distinguish all LGG and HGG samples by computing the intra-biopsy diffCCO con-
130 centration mean ($p=0.017$), despite visible overlap (with overlap coefficient of 61%) between the
131 distributions as seen in Fig. 5c. Singularly, we also reported that both oxCCO and redCCO indi-
132 vidualy are seemingly not able to distinguish biopsy grading, as we find overlap coefficients of
133 84.6% and 73.3%, and no statistically significant differences ($p=0.99$ and $p=0.12$, respectively).
134 This is shown in Fig. 6 plotting probability density distributions of each pixel across all biopsies,
135 divided between LGG and HGG. Only the difference diffCCO between the two inferred concen-
136 trations resulted in the suggested distinction of the two classes of tumoral grades.

137 Furthermore, as depicted in Fig. 5d, we also found an approximately linear correlation in the
138 2D domain between the mean differences in concentration of diffCCO and those of HbO_2 : together
139 with a reduced DiffCCO mean concentration, HGG samples also present a correlated reduction in

140 the mean concentration of HbO₂, with the combination of the two biomarkers enhancing the pos-
141 sibility of separating samples grading more effectively.



142 **Fig. 6** Histogram showing probability density distribution of inferred oxCCO (a) and redCCO (b) concentrations of
143 each pixel across different LGG (displayed in green) and HGG (displayed in red) grade samples. Neither the in-
144 ferred oxCCO and redCCO density distributions using the NIR range (740-900 nm) suggest to be able to differenti-
145 ate tumour grading, contrary to the diffCCO mean concentrations.

146

147 On a final note, we observed that the HGG sample S9 additionally displays diffCCO character-
148 istics close to LGG samples (Fig. 5d): we hypothesise that there could be different (possibly con-
149 current) reasons for this low distinguishability: even though it has not been shown that HGG sam-
150 ples can show characteristics of LGG samples, the opposite (i.e., high grade-typical histological
151 characteristics in low grade lesions) has recently been reported by Motomura *et al*²³. Thus, in gen-
152 eral, we suggest that it might be possible that lower grade lesions could display characteristics of
153 higher grade lesions, although further investigation on this would be needed.

154 4 Conclusions

155 We presented a novel, transportable HSI device, name HyperProbe1, based on fast spectral scan-
156 ning via a combination of SCL illumination and AOTF filtering. At full operational performances,

157 HyperProbel can scan sequentially up to 79 wavelengths between 510 and 900 nm, with 5-nm
158 sampling and high spectral resolution (3.5-7 nm of bandwidth), as well as acquire corresponding
159 spectral images on a 0.9 x 0.9-cm² FOV at high spatial resolution (4.38 μ m), in less than 5 minutes.

160 Furthermore, we also provided a preliminary assessment of the data acquired and analysed with
161 HyperProbel on a number (n = 11) of fresh surgical samples of glioma from patients at different
162 WHO gradings, including both lower grade (WHO grades II and III) and higher grades (WHO
163 grade IV) tumours. The initial findings demonstrated the capability of the device to reconstruct
164 quantitative maps of the distribution of the concentrations of various chromophores of interest, in
165 particular haemoglobin and CCO (both established biomarkers for tissue haemodynamics and me-
166 tabolism, respectively), as well as lipids volumetric content. We also looked at differences in the
167 inferred contributions of these biomolecules between LGG and HGG biopsies, that may suggest a
168 way to distinguish between the two, and thus potentially provide the basis for a HSI-based meth-
169 odology for tumour classification. We found indeed significant differences between mean lipid
170 contents across samples that could potentially be used to distinguish tumour grading, when fitting
171 over the entire work range (510-900 nm). In particular, HGGs presented higher mean lipid content
172 than LGGs: a plausible biological interpretation of this could be connected to a substantial lipid
173 storage for lipid metabolism in higher grade gliomas, a known characteristic feature of GBM^{24,25}.

174 Similarly, we also found that the analysed HGGs presented inferior concentrations of diffCCO
175 compared to LGGs, when fitting the data exclusively in the NIR range (740-900 nm): this may
176 suggest a potential metabolic path with NIR light to distinguish lower and higher grade samples.
177 This finding may also emphasise the potential role of diffCCO in providing metabolic differences
178 that lies beyond its critical use in NIR spectroscopy (NIRS) applications¹⁷. The exact mechanisms
179 by which these concentration differences in diffCCO arise still remain uncertain: as changes in the

180 concentration of diffCCO are directly proportional to variations in the metabolic activity of the
181 tissue, one would expect an influence of enhanced hypermetabolism in tumours at higher grades.
182 However, HGGs (such as GBMs) are characterised by the unique presence of necrotic tissue as
183 the core part of the lesion, with the hypermetabolic region occurring only at the borders^{26,27}. Such
184 central necrotic areas, composed almost entirely of dead -i.e., ametabolic- cells could explain the
185 overall reduced mean concentration of diffCCO in HGG compared to LGG, which instead do not
186 present necrosis. Furthermore, the results showed a direct correlation between the reduction of
187 diffCCO in HGG with a corresponding decrease in HbO₂, which could also be connected to the
188 hypoxic microenvironment that is specific of this type of brain tumours^{28,29}. From a biological
189 perspective, HGGs, such as GBMs, are known to be triggered and driven in their proliferation by
190 hypoxic microenvironments within the cerebral tissue^{28,29}. Such phenomenon could explain the
191 reduced mean concentration of HbO₂, which is a biomarker for oxygenation of the brain, and its
192 correlation with the diffCCO, since a direct association between oxygen delivery and its metabolic
193 consumption has been strongly established³⁰.

194 Future investigations on a larger and enriched cohort of biopsy samples of various types will
195 be needed to further confirm all these results on a more robust statistical basis. In particular, com-
196 parisons with control samples composed of healthy cerebral tissue will also be strongly required
197 for increasing the accuracy and reliability of any prediction.

198 The goal of HyperProbe1 is to provide a first proof-of-concept application to rapid and quanti-
199 tative digital histology of *ex vivo* tissue from excised surgical biopsies, in particular of cerebral
200 glioma, by reconstructing quantitative maps of the distributions of chromophores of interest in the
201 tissue via fast spectral unmixing algorithms. In this perspective, we demonstrated that Hy-
202 perProbe1 can collect and analyse full-range HSI data of light reflectance from surgical biopsies

203 in less than 1 hour after their excision (including preparation of the sample and setting up of the
204 measurements), a significantly much faster time than traditional H&E histopathological screening,
205 which normally takes several days up to few weeks. Such result qualifies HyperProbe1 for an
206 envisioned, future utilisation providing *in situ*, streamlined, and non-destructive screening of fresh
207 tissue samples, ideally within or just next to the operating theatre. This application could consid-
208 erably benefit the outcome of the surgical treatment and provide an all-optical advancement to
209 current post-surgical histopathological practice.

210 From a technological perspective, we also aim and improving the current setup of HyperProbe1
211 to further improve its performances: we are currently working on extending the operational spec-
212 tral range of the device at both ends, by (1) covering the rest of the available visible range below
213 500 nm and including also part of the near ultraviolet (UV), as well as by (2) expanding the NIR
214 coverage beyond 900 nm. This approach could further enrich the collected spectral data and allow
215 us to potentially target even additional chromophores of interest⁸.

216 The versatility of HyperProbe1 could also pave the way for potential applications of the instru-
217 mentation to virtually any types of surgical and non-surgical biopsy (or other *ex vivo* tissues), as
218 well as even move beyond digital histopathology. In this perspective, HyperProbe1 can also be
219 envisioned as an investigative, high-performances HSI device for preclinical *in vivo* applications:
220 it could be used to explore and tailor features of HSI (such as type and number of wavelengths)
221 that could be translated into clinical settings by specifically engineering more compact, cost-effec-
222 tive and user-friendly medical devices. Within the framework of the HyperProbe project and con-
223 sortium^{31,32}, we indeed aim at translating this technology for its use as a new neuronavigation tool
224 during brain surgery, such as in glioma resection. Such a device would aim at providing an inno-
225 vative approach to guided-neurosurgery, by transforming current practice towards an all-optical,

226 real-time, quantitative and accurate imaging approach, that could significantly help neurosurgeons,
227 enhance the efficacy of the treatment, and ultimately improve life expectancy of the patients.

228 *Disclosures*

229 The authors declare no financial conflict of interest.

230 *Code, Data, and Materials*

231 In support of open science, the data presented in this article are publicly available on Zenodo at
232 <https://zenodo.org/records/10908359>. Similarly, all our spectral unmixing code is available on
233 GitHub at <https://github.com/HyperProbe/SpectraFit>.

234 *Acknowledgments*

235 The HyperProbe consortium and project has received funding from the European Union’s Horizon
236 Europe research and innovation program under grant agreement No 101071040 – Project Hy-
237 perProbe. Views and opinions expressed are however those of the author(s) only and do not nec-
238 essarily reflect those of the European Union. Neither the European Union nor the granting author-
239 ity can be held responsible for them. AA, FL and IL from UCL are supported by UK Research and
240 Innovation (UKRI) grant No. 10048387

241 *References*

- 242 1. M. Titford, “A short history of histopathology technique,” *J. Histotechnol.* **29**(2), 99–110 (2006)
243 [doi:[10.1179/his.2006.29.2.99](https://doi.org/10.1179/his.2006.29.2.99)].
- 244 2. N. Sanai and M. S. Berger, “Surgical oncology for gliomas: The state of the art,” *Nat. Rev. Clin.*
245 *Oncol.* **15**(2), 112–125 (2018) [doi:[10.1038/nrclinonc.2017.171](https://doi.org/10.1038/nrclinonc.2017.171)].
- 246 3. P. Kleihues et al., “Histopathology, classification, and grading of gliomas,” in *Glia* **15**(3), pp. 211–

- 247 221, John Wiley & Sons, Ltd (1995) [doi:[10.1002/glia.440150303](https://doi.org/10.1002/glia.440150303)].
- 248 4. M. Weller et al., “Glioma,” *Nat. Rev. Dis. Prim.* **1**(1), 1–18 (2015) [doi:[10.1038/nrdp.2015.17](https://doi.org/10.1038/nrdp.2015.17)].
- 249 5. A. Tarsitano et al., “Intraoperative biopsy of the major cranial nerves in the surgical strategy for
250 adenoid cystic carcinoma close to the skull base,” *Oral Surg. Oral Med. Oral Pathol. Oral Radiol.*
251 **113**(2), 214–221, Mosby (2012) [doi:[10.1016/j.tripleo.2011.02.014](https://doi.org/10.1016/j.tripleo.2011.02.014)].
- 252 6. M. J. Van Den Bent, “Interobserver variation of the histopathological diagnosis in clinical trials on
253 glioma: A clinician’s perspective,” *Acta Neuropathol.* **120**(3), 297–304 (2010)
254 [doi:[10.1007/s00401-010-0725-7](https://doi.org/10.1007/s00401-010-0725-7)].
- 255 7. G. Lu and B. Fei, “Medical hyperspectral imaging: a review,” *J. Biomed. Opt.* **19**(1), 010901
256 (2014) [doi:[10.1117/1.JBO.19.1.010901](https://doi.org/10.1117/1.JBO.19.1.010901)].
- 257 8. L. Giannoni, F. Lange, and I. Tachtsidis, “Hyperspectral imaging solutions for brain tissue
258 metabolic and hemodynamic monitoring: past, current and future developments,” *J. Opt.* **20**(4),
259 044009 (2018) [doi:[10.1088/2040-8986/aab3a6](https://doi.org/10.1088/2040-8986/aab3a6)].
- 260 9. L. Giannoni, F. Lange, and I. Tachtsidis, “Investigation of the quantification of hemoglobin and
261 cytochrome-c-oxidase in the exposed cortex with near-infrared hyperspectral imaging: a
262 simulation study,” *J. Biomed. Opt.* **25**(04), 1 (2020) [doi:[10.1117/1.JBO.25.4.046001](https://doi.org/10.1117/1.JBO.25.4.046001)].
- 263 10. L. Giannoni et al., “A hyperspectral imaging system for mapping haemoglobin and cytochrome-c-
264 oxidase concentration changes in the exposed cerebral cortex,” *IEEE J. Sel. Top. Quantum*
265 *Electron.* **27**(4), 7400411 (2021) [doi:[10.1109/JSTQE.2021.3053634](https://doi.org/10.1109/JSTQE.2021.3053634)].
- 266 11. L. Giannoni et al., “Optical characterisation and study of ex vivo glioma tissue for hyperspectral
267 imaging during neurosurgery,” *Proc. SPIE 12628, Diffus. Opt. Spectrosc. Imaging IX*(1262829),
268 153–159 (2023) [doi:[10.1117/12.2670854](https://doi.org/10.1117/12.2670854)].
- 269 12. U. Khan et al., “Trends in Deep Learning for Medical Hyperspectral Image Analysis,” *IEEE*
270 *Access* **9**, 79534–79548 (2021) [doi:[10.1109/ACCESS.2021.3068392](https://doi.org/10.1109/ACCESS.2021.3068392)].
- 271 13. G. Florimbi et al., “Towards Real-Time Computing of Intraoperative Hyperspectral Imaging for
272 Brain Cancer Detection Using Multi-GPU Platforms,” *IEEE Access* **8**, 8485–8501 (2020)

- 273 [doi:[10.1109/ACCESS.2020.2963939](https://doi.org/10.1109/ACCESS.2020.2963939)].
- 274 14. D. N. Louis et al., “The 2021 WHO classification of tumors of the central nervous system: A
275 summary,” *Neuro. Oncol.* **23**(8), 1231–1251, Neuro Oncol (2021) [doi:[10.1093/neuonc/noab106](https://doi.org/10.1093/neuonc/noab106)].
- 276 15. F. Lange, L. Giannoni, and I. Tachtsidis, “The Use of Supercontinuum Laser Sources in
277 Biomedical Diffuse Optics: Unlocking the Power of Multispectral Imaging,” *Appl. Sci.* **11**(10),
278 4616 (2021) [doi:[10.3390/APP11104616](https://doi.org/10.3390/APP11104616)].
- 279 16. I. Ezhov et al., “Shallow learning enables real-time inference of molecular composition changes
280 from broadband-near-infrared spectroscopy of brain tissue,” *arXiv: 2309.16735* (2024).
- 281 17. G. Bale, C. E. Elwell, and I. Tachtsidis, “From Jöbsis to the present day: a review of clinical near-
282 infrared spectroscopy measurements of cerebral cytochrome-c-oxidase,” *J. Biomed. Opt.* **21**(9),
283 091307 (2016) [doi:[10.1117/1.JBO.21.9.091307](https://doi.org/10.1117/1.JBO.21.9.091307)].
- 284 18. S. L. Jacques, “Optical properties of biological tissues: a review,” *Phys. Med. Biol.* **58**(11), R37–
285 R61, IOP Publishing (2013) [doi:[10.1088/0031-9155/58/11/R37](https://doi.org/10.1088/0031-9155/58/11/R37)].
- 286 19. S. A. Prahl, “Optical absorption of hemoglobin,” 1999, <<http://omlc.org/spectra/hemoglobin>>.
- 287 20. Q. Fang and D. A. Boas, “Monte Carlo Simulation of Photon Migration in 3D Turbid Media
288 Accelerated by Graphics Processing Units,” *Opt. Express* **17**(22), 20178, Optical Society of
289 America (2009) [doi:[10.1364/OE.17.020178](https://doi.org/10.1364/OE.17.020178)].
- 290 21. L. Yu et al., “Scalable and massively parallel Monte Carlo photon transport simulations for
291 heterogeneous computing platforms,” *J. Biomed. Opt.* **23**(01), 1, Society of Photo-Optical
292 Instrumentation Engineers (2018) [doi:[10.1117/1.jbo.23.1.010504](https://doi.org/10.1117/1.jbo.23.1.010504)].
- 293 22. A. N. Yaroslavsky et al., “Optical properties of selected native and coagulated human brain tissues
294 in vitro in the visible and near infrared spectral range,” *Phys. Med. Biol.* **47**(12), 2059–2073, IOP
295 Publishing (2002) [doi:[10.1088/0031-9155/47/12/305](https://doi.org/10.1088/0031-9155/47/12/305)].
- 296 23. K. Motomura et al., “Clinical characteristics and radiological features of glioblastoma, IDH-
297 wildtype, grade 4 with histologically lower-grade gliomas,” in *Brain Tumor Pathology* **40**(2), pp.
298 48–55, Springer (2023) [doi:[10.1007/s10014-023-00458-5](https://doi.org/10.1007/s10014-023-00458-5)].

- 299 24. Y. Kou, F. Geng, and D. Guo, “Lipid Metabolism in Glioblastoma: From De Novo Synthesis to
300 Storage,” in *Biomedicines* **10**(8), p. 1943, Multidisciplinary Digital Publishing Institute (2022)
301 [doi:[10.3390/biomedicines10081943](https://doi.org/10.3390/biomedicines10081943)].
- 302 25. E. Verdugo, I. Puerto, and M. Á. Medina, “An update on the molecular biology of glioblastoma,
303 with clinical implications and progress in its treatment,” in *Cancer Communications* **42**(11), pp.
304 1083–1111, John Wiley & Sons, Ltd (2022) [doi:[10.1002/cac2.12361](https://doi.org/10.1002/cac2.12361)].
- 305 26. L. Persano et al., “The three-layer concentric model of glioblastoma: Cancer stem cells,
306 microenvironmental regulation, and therapeutic implications,” *ScientificWorldJournal*. **11**, 1829–
307 1841, ScientificWorldJournal (2011) [doi:[10.1100/2011/736480](https://doi.org/10.1100/2011/736480)].
- 308 27. S. M. Markwell et al., “Necrotic reshaping of the glioma microenvironment drives disease
309 progression,” in *Acta Neuropathologica* **143**(3), pp. 291–310, Acta Neuropathol (2022)
310 [doi:[10.1007/s00401-021-02401-4](https://doi.org/10.1007/s00401-021-02401-4)].
- 311 28. A. R. Monteiro et al., “The role of hypoxia in glioblastoma invasion,” in *Cells* **6**(4), p. 45,
312 Multidisciplinary Digital Publishing Institute (2017) [doi:[10.3390/cells6040045](https://doi.org/10.3390/cells6040045)].
- 313 29. M. Domènech et al., “Hypoxia: The cornerstone of glioblastoma,” in *International Journal of*
314 *Molecular Sciences* **22**(22), p. 12608, Multidisciplinary Digital Publishing Institute (2021)
315 [doi:[10.3390/ijms222212608](https://doi.org/10.3390/ijms222212608)].
- 316 30. M. Caldwell et al., “Modelling blood flow and metabolism in the preclinical neonatal brain during
317 and following hypoxic-ischaemia,” *PLoS One* **10**(10), e0140171, Public Library of Science (2015)
318 [doi:[10.1371/journal.pone.0140171](https://doi.org/10.1371/journal.pone.0140171)].
- 319 31. L. Giannoni et al., “HyperProbe consortium: innovate tumour neurosurgery with innovative
320 photonic solutions,” in <https://doi.org/10.1117/12.2670764> **12628**, p. 47, SPIE (2023)
321 [doi:[10.1117/12.2670764](https://doi.org/10.1117/12.2670764)].
- 322 32. “HyperProbe – HyperProbe Project Website,” <<https://hyperprobe.eu/>> (accessed 27 March 2024).



Luca Giannoni is a postdoctoral researcher at the European Laboratory for Non-Linear Spectroscopy (LENS) of the University of Florence. He received his PhD in Medical Imaging from University College London (UCL) in 2020. His current research interests focus on developing cutting-edge optical microscopy systems for neuroimaging, as well as on designing and validating cost-effective, compact HSI devices for clinical translation. He is a member of SPIE.

328



Marta Marradi is a PhD student at the European Laboratory for Non-Linear Spectroscopy (LENS) of the University of Florence. Her work specifically focuses on the development of novel imaging systems based on both multispectral and hyperspectral techniques for biomedical applications, concentrating in the dermatologic and neurological fields.

333



Ivan Ezhov is a research scientist at the Institute of Artificial Intelligence in Medicine at the Technical University of Munich. His research focus is at the intersection of biophysical modelling, inverse problems, and deep learning. His interests include computational oncology, physics-based machine learning and spectral unmixing of large scale datasets, such as medical hyperspectral images.

338



Camilla Bonaudo is a neurosurgeon at the Azienda Ospedaliera of Careggi, and a PhD student in Neuroscience at the University of Florence. Her work focuses on the development of new protocols for the application of technologies, such as Navigated Transcranial Magnetic Stimulation (nTMS), to study cognitive functions, acquiring data about brain plasticity and functional reshaping. Her aim is to study brain connectome and comparing functional mapping with the gold standard of the Direct Cortical Simulation.

344

345



Angelos Artemiou is an MRes student at University College London (UCL), specializing in the field of Medical Physics and Biomedical Engineering. His research is primarily focused on developing novel phantoms for the metrological characterisation of NIR and hyperspectral instrumentation.



Anam Toaha is a PhD student at the European Laboratory for Non-Linear Spectroscopy (LENS) of the University of Florence. She conducts research in the field of biomedical imaging and spectroscopy. She is also part of the HyperProbe project, working on the development of a novel optical imaging device based on hyperspectral imaging, to advance brain surgery by

355 presenting neurosurgeons with enhanced information intraoperatively.



Frédéric Lange received his PhD from the University of Lyon and INSA de LYON in 2016. He is now a senior research associate with the Biomedical Optics Research Laboratory, Department of Medical Physics and Biomedical Engineering at University College London. His current main research interests are in the development of novel optical technologies to

361 monitor tissue's oxygenation and metabolism, with a specific interest for non-invasive brain mon-

362 itoring in healthy (i.e., brain development/neuroscience) and pathological conditions.



Bruno Montcel is a professor at University Claude Bernard Lyon 1. He leads research focused on optical medical devices at CREATIS laboratory and is the chairman of the Biomedical Engineering Department of Polytech Lyon. Its research explores optical imaging methods and experimental set up for the exploration of tissue physiology and pathologies. It mainly fo-

368 cuses on intraoperative and point of care hyperspectral optical imaging methods for medical diag-
369 nosis and gesture assistance.



Alessandro Della Puppa is a professor of neurosurgery, a neurosurgeon, and the head of the Neurosurgical Department at the Azienda Ospedaliera of Careggi, in Florence. His major interests concern the surgical improvement of neuro-oncology, in particular regarding the development of new intraoperative strategies in awake surgery, in immuno-neuro-oncology, and

375 in navigational TMS in the preoperative and intraoperative mapping of language and cognitive
376 functions, all aiming towards a patient-tailored rehabilitation program.



Ilias Tachtsidis is a professor at University College London. He leads the Multimodal Spectroscopy and MetaboLight groups in the Biomedical Optics Research Laboratory at the department of Medical Physics and Biomedical Engineering. Tachtsidis is a multidisciplinary scientist with a research portfolio encompassing engineering, physics, computing, neurosci-

382 ence and clinical medicine. His research focus is technology development in optical neuroimaging
383 (devices, algorithms), through applications (clinical, neuroscience), to data analytics towards gen-
384 erating clinical information and knowledge (computational models).



Daniel Rückert is Alexander von Humboldt Professor for artificial intelligence (AI) in Medicine and Healthcare at the Technical University of Munich, where he directs the Institute for AI and Informatics in Medicine. He is also a professor in the Department of Computing at Imperial College London. From 2016 to 2020 he served as Head of the Department at Imperial

390 College. His research focuses on medical image computing, data science and AI in medicine.



Francesco Saverio Pavone is a professor at the University of Florence. He is the director of the Biophotonics area at the European Laboratory for Non-Linear Spectroscopy, focusing on optical microscopy and imaging. Pavone is also coordinator of several EU projects, including the HyperProbe consortium. He participates in the NIH BRAIN initiative and

396 HBP Brain Initiative. He is also the Italian node leader of EBRAIN and the Italian delegate in the
397 Board of Directors of EuroBioImaging.

398 Biographies and photographs for the other authors are not available.

399

400 **Caption List**

401

402 **Fig. 1** (a) Schematics of HyperProbe1; (b) Picture of the illumination side of HyperProbe1; (c)
403 Picture of the imaging side of HyperProbe1; (d) Testing of the spatial resolution of HyperProbe1;
404 (e) Line profile of the smallest resolved element; (f) Example of glioma biopsy sample.

405 **Fig. 2** (a) Absorption coefficients for HbO₂, HHb, lipids and water, and scattering coefficient of
406 generic brain tissue; b) Molar extinction coefficients of HbO₂, HHb, oxCCO and redCCO; c) Sim-
407 ulated fluence rates within the 3D biopsy model at different wavelengths; d) Simulated mean pho-
408 ton pathlength within the 3D biopsy model, as a function of wavelength; e) Partial pathlength
409 distributions of the photons simulated within the 3D biopsy model at various wavelengths.

410 **Fig. 3** (a) Intercomparison between average reflectance spectra across all samples; (b) Comparison
411 of average reflectance spectra between LGG and HGG samples; (c) Example of spectral frame at
412 560 nm, acquired with HyperProbe1 on biopsy sample S2; (d) Example of average reflectance
413 spectra in different ROIs of the HyperProbe1 data; (e) Example of average attenuation spectra in
414 different ROIs of the HyperProbe1 data;

415 **Fig. 4** Spectral fit and corresponding inferred HbT and diffCCO concentration maps of both a

416 HGG (a) and a LGG sample (b), fitting the whole wavelength spectrum (510-900 nm); (c) Histo-
417 gram showing density distribution of inferred lipid content of each pixel across different LGG and
418 HGG samples; (d) Distribution means of the lipid contents and diffCCO concentrations suggest
419 that lipid mean content could be able to distinguish grading of all samples, whereas no apparent
420 separation is visible for the inferred mean diffCCO concentrations.

421 **Fig. 5** Spectral fit and corresponding inferred HbT and diffCCO concentration maps of both a
422 HGG (a) and a LGG sample (b), fitting exclusively the NIR range (740-900 nm); (c) Histogram
423 showing density distribution of inferred diffCCO concentrations of each pixel across different
424 LGG and HGG samples; (d) Distribution means of diffCCO and HbO₂ concentrations suggest that
425 these parameters could be able to distinguish LGG and HGG samples of glioma tissue, with
426 diffCCO being the most accurate, across all the samples.

427 **Fig. 6** Histogram showing probability density distribution of inferred oxCCO (a) and redCCO (b)
428 concentrations of each pixel across different LGG (displayed in green) and HGG (displayed in
429 red) grade samples, showing no significance differences in either cases for the range 740-900 nm.

430 **Table 1** List of components of HyperProbe1 with specifications.

431 **Table 2** Technical characteristics and features of HyperProbe1.

432 **Table 3** Classification of the tissue samples investigated with HyperProbe1.

433 **Table 4** Composition of the 3D in silico model of brain biopsy used for the MC simulations.